Signatures of beta-sheet secondary structures in linear and two-dimensional infrared spectroscopy

Cheatum, Christopher M.; Tokmakoff, Andrei; Knoester, Jasper

Published in:
Journal of Chemical Physics

DOI:
10.1063/1.1689637

Publication date:
2004

Signatures of β-sheet secondary structures in linear and two-dimensional infrared spectroscopy

Christopher M. Cheatum[a] and Andrei Tokmakoff[a]
Department of Chemistry, Massachusetts Institute of Technology, Cambridge, Massachusetts 02139

Jasper Knoester
Materials Science Centre, University of Groningen, Nijenborgh 4, 9747 AG Groningen, The Netherlands

(Received 5 December 2003; accepted 3 February 2004)

Using idealized models for parallel and antiparallel β sheets, we calculate the linear and two-dimensional infrared spectra of the amide I vibration as a function of size and secondary structure. The model assumes transition–dipole coupling between the amide I oscillators in the sheet and accounts for the anharmonic nature of these oscillators. Using analytical and numerical methods, we show that the nature of the one-quantum vibrational eigenstates, which govern the linear spectrum, is, to a large extent, determined by the symmetry of the system and the relative magnitude of interstrand interactions. We also find that the eigenstates, in particular their trends with system size, depend sensitively on the secondary structure of the sheet. While in practice these differences may be difficult to distinguish in congested linear spectra, we demonstrate that they give rise to promising markers for secondary structure in the two-dimensional spectra. In particular, distinct differences occur between the spectra of parallel and antiparallel β sheets and between β hairpins and extended β sheets. © *2004 American Institute of Physics.* [DOI: 10.1063/1.1689637]

I. INTRODUCTION

Investigations into the vibrational spectroscopy of proteins over several decades have shown that the infrared transitions associated with the amide bands of the polypeptide backbone are sensitive to the structure of the protein.[1,2] The amide I spectrum, arising primarily from the peptide CO stretch, shows frequency shifts that are empirically related to the presence of secondary structural elements.[1–4] This structural sensitivity arises from the vibrational couplings between the amide I oscillators which depend on the relative position, orientation, and connectivity of the peptide units. Other factors also influence protein infrared spectra, such as configurational disorder, hydrogen bonding within the protein or to the solvent, and fast vibrational relaxation. These effects broaden infrared absorption spectra resulting in featureless bands that are difficult to interpret in terms of the underlying protein structure.

The infrared absorption spectrum contains information about all of the structural and dynamical variables that influence the vibrational states of the protein, but it is impossible to separate and isolate each of these contributions to the spectrum. Two-dimensional infrared (2DIR) spectroscopy, a third-order nonlinear spectroscopy, provides a means to dissect congested IR spectra.[5,6] A 2DIR spectrum spreads resonances over two frequency dimensions revealing vibrational couplings through the formation of cross peaks and separating overlapping or inhomogeneous contributions that complicate the linear spectrum.[7–11] 2DIR spectroscopy also measures the angles between pairs of transition dipole vectors,[12,13] and characterizes correlated frequency shifts between transitions.[7,14–19]

The potential of 2DIR spectroscopy has generated renewed interest in understanding the IR spectra of peptides and proteins and in approaches to calculating the couplings between amide I oscillators. Most notably, a number of 2DIR studies of small peptides in solution have used amide I couplings to extract peptide conformation and conformational dynamics.[14,18,20–26] For some small dipeptide systems, new models for the amide I coupling have been compared to direct *ab initio* calculations of the coupling matrix elements.[27–30] For modestly larger systems, *ab initio* calculations for smaller portions of the system can be combined to build up a model of the spectroscopy.[31–33] These investigations are providing a better description of the influence of the local configuration and bonding on amide vibrational couplings. Although studies on larger systems with secondary structure exist,[23,26] there have been no systematic 2DIR investigations on proteins, because the interpretation of IR spectra for complex secondary and tertiary structures is still quite difficult. Most proteins are large enough that directly calculating the 2DIR spectrum is too computationally expensive. Even if the computational challenges are overcome, there is little insight available from a brute-force calculation of the spectrum.

As an initial step in analyzing protein 2DIR spectroscopy, we investigate idealized models for the vibrational spectroscopy of β sheets and β hairpins, two common secondary structures in proteins. The amide I spectrum of antiparallel β sheets is of particular interest because two transitions are observed in the amide I spectrum, suggesting that there will be a distinct cross peak in the 2DIR spectrum. We treat β sheets of varying geometry as idealized secondary structures of periodically repeating peptide units. We calcu-

[a]Also at Materials Science Center, University of Groningen, Groningen, The Netherlands.

late the one- and two-quantum vibrational eigenstates both using periodic boundary conditions, taking advantage of translational symmetry to reduce the computational effort, and by directly diagonalizing the Hamiltonian for finite systems with open boundary conditions. We calculate the linear and 2DIR spectra focusing on the variation of spectral features with structure and size and identifying the important interactions that determine the trends in the spectra. We use simple electrostatics to model the vibrational couplings, but the essential results depend on the pattern of couplings and not on the quantitative details of the interactions.

Elements of the model and the calculations of the nonlinear response borrow from a number of earlier studies. Our work builds on an early description of amide I spectroscopy introduced by Miyazawa, in which vibrations of parallel and antiparallel β sheets and α helices were studied using periodic boundary conditions and interactions between nearest-neighbor amide I oscillators.[34,35] We use the transition dipole coupling model parametrized by Krimm and co-workers[1] to describe the interactions between amide I oscillators. This approach provides reasonable agreement between measured and calculated infrared spectra of proteins[1,36–39] and models of β sheets similar to the one we use.[40,41] Our approach to calculating the 2DIR spectra builds on previous studies of the pump-probe spectroscopy of electronic transitions in molecular aggregates.[42–47] We have extended this approach, deriving expressions for the third-order nonlinear vibrational response functions for multilevel anharmonic oscillators.

The paper is presented as follows. In Sec. II we present the model we use to calculate the singly and doubly excited vibrational states. We outline the calculations of the linear spectra and polarization-selective 2DIR spectra in Sec. III. Section IV describes analytical solutions for the one-quantum eigenstates for certain geometries and compares those results with numerical solutions. We show calculated linear and 2DIR spectra in Sec. V, and we discuss the features of the spectrum, the influence of coupling and line-broadening mechanisms, and the spectral signatures of beta-sheet structures in Secs. V–VII. In Sec. VIII we summarize our conclusions.

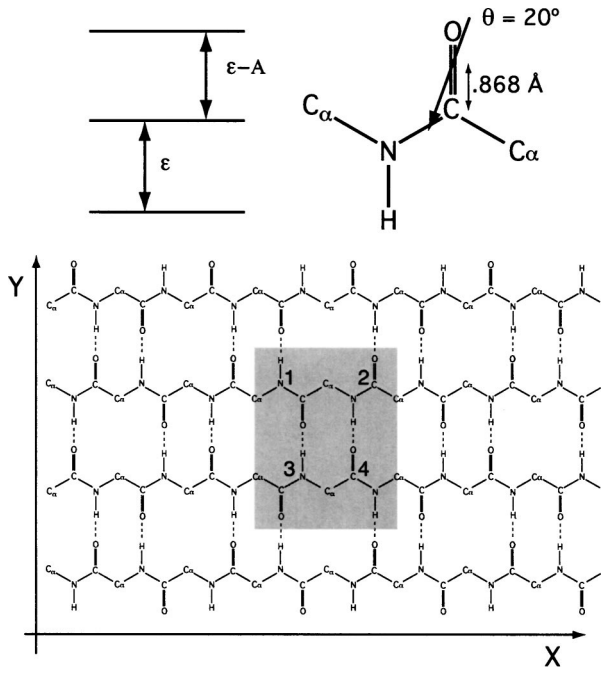

FIG. 1. Schematic representation of the model for antiparallel β sheets. The top left shows the energy level diagram for the oscillators. We assume $\epsilon = 1675\ \mathrm{cm}^{-1}$ and $A = 16\ \mathrm{cm}^{-1}$. The top-right corner depicts the position and orientation of the transition dipole vector we use to calculate the couplings between oscillators and the optical response. The bottom part of the figure shows the structural model for the antiparallel β sheets as seen from above the sheet. The shaded region corresponds to one unit cell, and the amide groups within that unit cell are distinguished by the label s (=1, 2, 3, and 4) as indicated. Larger sheets are constructed by increasing numbers of unit cells in the X or Y directions.

II. MODEL AND COLLECTIVE EIGENSTATES

A. Model Hamiltonian

We are interested in the infrared spectra of β sheets associated with the amide I vibration. This vibrational mode, in a single peptide unit, is composed primarily of CO stretching and is uncoupled from the side chain, so that each peptide unit represents an equivalent amide I oscillator. The fundamental transition energy of a single oscillator is denoted ϵ. Due to the anharmonic nature of the oscillator, the two-quantum state is redshifted by an amount A relative to 2ϵ. The corresponding three-level diagram for the single oscillator is depicted in the upper part of Fig. 1, together with the position and orientation of its effective transition dipole. In a β sheet with $N+1$ amino acids, there are N peptide bonds and therefore N amide I oscillators. These oscillators are coupled by electrostatic and through-bond interactions, which cause the eigenmodes to take on a collective character spread over several, possibly many, peptide bonds. This mixing leads to shifts in the optically allowed energy levels away from the single peptide transitions. The interactions depend on the arrangement of the peptide units in the sheet. We are mostly interested in antiparallel β sheets and restrict the theoretical analysis to this arrangement. Parallel sheets may be treated with minor modifications; some of the salient differences with antiparallel sheets are mentioned at the end of Sec. V.

We consider the antiparallel β-sheet structure displayed in Fig. 1, with canonical ϕ/ψ angles $(-160°, 118°)$ and with strands spaced so that the hydrogen bond length is 3.04 Å, where the length of the hydrogen bond is defined as the distance between amide N and O atoms on opposite strands.[48] The idealized antiparallel sheet may be regarded as a regular two-dimensional lattice with a unit cell that includes the four oscillators in the shaded region of Fig. 1. We take the X (Y) direction parallel (perpendicular) to the strands. An arbitrary sheet may now be indicated by the number of unit cells in each direction, as an $N_x \times N_y$ system. In this language, a hairpin is an $N_x \times 1$ system; in all other cases, we speak of an extended sheet. A particular oscillator in the sheet is labeled $\mathbf{n}s$, where $\mathbf{n}=(n_x,n_y)$ is a two-dimensional vector labeling the position of the unit cell and $s=1,...,4$ labels the members of the unit cell according to the convention in Fig. 1.

Restricting ourselves to one- and two-quantum states,

the Hamiltonian for the sheet of interacting oscillators may be written

$$H=\sum_{\mathbf{n}s}\epsilon a^{\dagger}_{\mathbf{n}s}a_{\mathbf{n}s}+\sum_{\mathbf{n}s,\mathbf{n}'s'}{}' L_{s,s'}(\mathbf{n}-\mathbf{n}')a^{\dagger}_{\mathbf{n}s}a_{\mathbf{n}'s'} -\frac{A}{2}\sum_{\mathbf{n}s} a^{\dagger}_{\mathbf{n}s}a^{\dagger}_{\mathbf{n}s}a_{\mathbf{n}s}a_{\mathbf{n}s}, \quad (1)$$

where the summations over $\mathbf{n}s$ and $\mathbf{n}'s'$ run over all oscillators in the sheet, and the operators $a^{\dagger}_{\mathbf{n}s}$ and $a_{\mathbf{n}s}$ denote the usual raising and lowering operators, respectively, for the oscillator $\mathbf{n}s$. The first term in Eq. (1) denotes the harmonic single-oscillator contribution, the second term represents the pairwise coupling between oscillators (the prime on the summation excludes self-interactions, i.e., terms with $\mathbf{n}=\mathbf{n}'$ if $s=s'$), while the last term accounts for the anharmonic nature of the single oscillator. We use the parameters $\epsilon=1675\ \mathrm{cm}^{-1}$ and $A=16\ \mathrm{cm}^{-1}$.[23,26,38,49] The value for ϵ is slightly larger than the usual frequency for amide I oscillators in proteins, but consistent with the computational analysis of absorption spectra measured for a series of proteins by Torii and Tasumi.[38] Changing the value of the zeroth-order frequency moves all of the bands in the linear spectrum by the same amount, but it does not affect the general trends or the splittings. Finally, we determine the pairwise interactions between oscillators using the transition dipole coupling model, which treats the electrostatic interaction between point transition dipoles of the amide I oscillators as the main source of coupling. This approximation neglects any ''through-bond'' interactions and will also break down if the peptide units are located too close together. In spite of these shortcomings, the transition dipole model provides reasonable agreement between measured and calculated infrared spectra of proteins.[1,36–41] To apply the model we assign a point dipole to each amide I oscillator. For each peptide unit, the dipole origin lies 0.868 Å from the carbonyl carbon on the CO bond axis and the dipole vector lies in the amide NCO plane 20° off of the CO bond axis toward the nitrogen as shown in Fig. 1.[1] The expression for the interaction energy of the dipoles is

$$L_{s,s'}(\mathbf{n}-\mathbf{n}')=C\left(\frac{\hat{\mu}_s\cdot\hat{\mu}_{s'}}{|\mathbf{r}_{\mathbf{n}s,\mathbf{n}'s'}|^3} -3\frac{(\hat{\mu}_s\cdot\mathbf{r}_{\mathbf{n}s,\mathbf{n}'s'})(\hat{\mu}_{s'}\cdot\mathbf{r}_{\mathbf{n}s,\mathbf{n}'s'})}{|\mathbf{r}_{\mathbf{n}s,\mathbf{n}'s'}|^5}\right), \quad (2)$$

where $\hat{\mu}_s$ is the unit vector in the direction of the transition dipole moment of the sth oscillator in the unit cell (see Table I), $\mathbf{r}_{\mathbf{n}s,\mathbf{n}'s'}$ is the relative position vector connecting the dipoles, and C is a constant that scales the magnitude of the interactions. In units where the energy of interaction is expressed in wave numbers and distances in Å, we use $C=580\ \mathrm{cm}^{-1}\ \mathrm{Å}^3$. The unit-cell dimensions are 6.879 Å in the x direction and 10.080 Å in the y direction consistent with the structural constraints of repeated units in the strand along the x direction and consistent with hydrogen bond lengths in the y direction.

For future reference and understanding, it is useful to give the values of the dominant interactions in the antiparallel β sheet within the transition dipole coupling model. The top part of Fig. 2 gives all interactions that exist within a single unit cell, the center part gives the dominant additional interactions between oscillators belonging to different unit cells for a hairpin configuration, while the bottom part gives the dominant additional interactions introduced in an extended sheet. The numbers illustrate that in general the interactions between unit cells in a hairpin are weak as compared to those within a single unit cell; the interactions along

TABLE I. Orientations and positions of the transition dipoles vectors of each of the oscillators in the single unit cell. The positions are given as a Cartesian vector corresponding to the position of the point dipole relative to an arbitrary origin in units of Å. The orientations are given as a unit Cartesian vector pointing in the direction of the transition dipole moment for the oscillator.

Oscillator	Dipole ($\hat{\mu}$)	Position ($\mathbf{r}$)
1	$-.288\hat{x}+.951\hat{y}+0.116\hat{z}$	$-1.233\hat{x}+1.154\hat{y}-.237\hat{z}$
2	$-.278\hat{x}-.950\hat{y}-.140\hat{z}$	$2.192\hat{x}+3.905\hat{y}+.237\hat{z}$
3	$.278\hat{x}+.950\hat{y}-.140\hat{z}$	$-2.192\hat{x}-3.905\hat{y}+.237\hat{z}$
4	.288x−.951y+.116z	$1.233\hat{x}-1.154\hat{y}-.237\hat{z}$

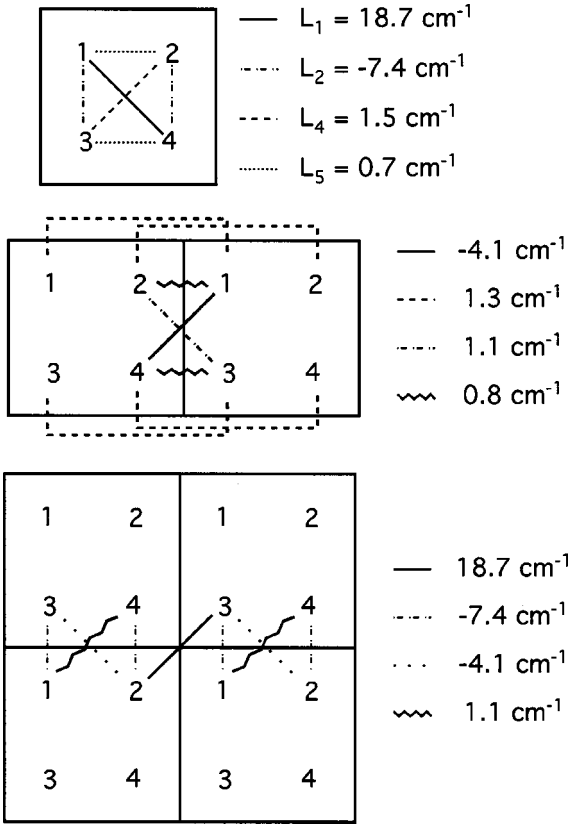

FIG. 2. (Top) The pairwise interactions between oscillators within the unit cell. The numbers inside the box index the members of the unit cell. Each of the interactions is represented by a line with equivalent lines indicating equivalent interactions. The numbers to the right of the diagram are the magnitudes of the couplings for our parametrization of the transition dipole model. (Middle) Additional interactions present in the hairpin for nearest-neighbor unit cells. (Bottom) The dominant interactions present in extended sheets. These interactions are in addition to all of the interactions shown above. Again, the magnitudes of the interactions are given to the right of the figure.

strands (i.e., between molecules 1 and 2, or 3 and 4) are particularly weak.

B. One- and two-quantum vibrational eigenstates

To calculate infrared absorption spectra for a sheet of $N=4N_xN_y$ oscillators, we need the N one-quantum eigenstates of the Hamiltonian Eq. (1). These follow from the diagonalization of the sub-block of the Hamiltonian Eq. (1) that acts within the space of states with one vibrational quantum. In the site representation, the basis of this space is formed by the states $a^\dagger_{\mathbf{n}s}|g\rangle$, where $|g\rangle$ is the ground state (no vibrational quanta) and $\mathbf{n}s$ runs over all molecules. In the site basis, the $N\times N$ one-quantum block of the Hamiltonian has all diagonal elements equal to ϵ, while the off-diagonal elements are given by the interactions $L_{s,s'}(\mathbf{n}-\mathbf{n}')$. The anharmonicity does not affect this block. Each one-quantum eigenstate $|b\rangle$ is a linear combination of site states, with coefficients given by the components $\phi_{\mathbf{n}s}(b)$ of one of the eigenvectors of the one-quantum Hamiltonian matrix. The corresponding eigenvalue E_b gives the energy of the state. For the optical response, the transition dipole matrix elements from the ground state to the one-quantum eigenstates are important. They are given by $\boldsymbol{\mu}_b=\langle b|\mathbf{M}_+|g\rangle$, with $\mathbf{M}_+=\Sigma_{\mathbf{n}s}\boldsymbol{\mu}_{\mathbf{n}s}a^\dagger_{\mathbf{n}s}$, the total dipole operator of the sheet associated with adding one quantum to the system. One thus easily shows that the dipole matrix elements are given by $\boldsymbol{\mu}_b=\Sigma_{\mathbf{n}s}\boldsymbol{\mu}_s\phi_{\mathbf{n}s}(b)$. Here, $\boldsymbol{\mu}_s=\mu\hat{\mu}_s$, μ being the magnitude of the dipole associated with the amide I vibration, and $\hat{\mu}_s$ as given in Table I.

Two-dimensional spectroscopy reveals the magnitude of vibrational couplings by probing the frequency of vibrational transitions between the singly excited vibrational states and doubly excited states involving two modes, i.e., combination bands. Therefore simulation of 2DIR spectra requires knowledge of the $N(N+1)/2$ two-quantum states. These follow from diagonalizing the $N(N+1)/2$ dimensional two-quantum sub-block of the Hamiltonian, which is easily generated in the site representation by calculating the matrix elements $\langle \mathbf{n}s\mathbf{n}'s'|H|\mathbf{n}''s''\mathbf{n}'''s'''\rangle$, with $|\mathbf{n}s\mathbf{n}'s'\rangle=ca^\dagger_{\mathbf{n}s}a^\dagger_{\mathbf{n}'s'}|g\rangle$ (c such that the state is normalized to unity). As a simple example, for a system existing of three oscillators, labeled 1, 2, and 3, the two-quantum subspace is six dimensional and within the site representation the Hamiltonian matrix in this subspace is given by

$$H^{(2)}=\begin{pmatrix} 2\epsilon-A & 0 & 0 & \sqrt{2}L_{12} & \sqrt{2}L_{13} & 0 \\ 0 & 2\epsilon-A & 0 & \sqrt{2}L_{12} & 0 & \sqrt{2}L_{23} \\ 0 & 0 & 2\epsilon-A & 0 & \sqrt{2}L_{13} & \sqrt{2}L_{23} \\ \sqrt{2}L_{12} & \sqrt{2}L_{12} & 0 & 2\epsilon & L_{23} & L_{13} \\ \sqrt{2}L_{13} & 0 & \sqrt{2}L_{13} & L_{23} & 2\epsilon & L_{12} \\ 0 & \sqrt{2}L_{23} & \sqrt{2}L_{23} & L_{13} & L_{12} & 2\epsilon \end{pmatrix}. \tag{3}$$

The general two-quantum eigenstate will be denoted $|c\rangle$, with energy E_c. Dipole allowed transitions states $|c\rangle$ do not exist from the ground state for the excitation energies we consider, but they do occur from the one-exciton states. In general, their dipoles are written $\boldsymbol{\mu}_{cb}=\langle c|\mathbf{M}_+|b\rangle$.

We refer to the explicit diagonalization of the one- and two-quantum Hamiltonians on a computer as the brute-force method of calculating the infrared spectra. An advantage of this method is that it is easily applied, even in the presence of disorder in the oscillator frequencies and interactions. A disadvantage is the numerical expense, not only because the two-quantum matrix even for moderate values of N gets very large, but even more so because the calculation of the two-dimensional response functions involves nested summations over one- and two-quantum eigenstates for each frequency pair (ω_1,ω_3) [cf. Eqs. (8) and (9)]. A second disadvantage of the brute-force method is its black-box character, which makes it harder to understand the spectra obtained.

Assuming an idealized sheet structure, with a perfect repetition of unit cells, and imposing periodic boundary conditions simplify the calculation of the eigenstates and spectra considerably (for hairpins this condition naturally is only used in the X direction). This periodicity immediately dictates Bloch forms for the one-quantum eigenstates, which, in analogy to the exciton states in molecular crystals, are given by[50]

$$|\mathbf{q}\sigma\rangle=N^{-1/2}\sum_{\mathbf{n}s}\phi_{\sigma s}(\mathbf{q})e^{i\mathbf{q}\cdot\mathbf{n}}a^\dagger_{\mathbf{n}s}|g\rangle. \tag{4}$$

Here, $\mathbf{q}$ denotes one of the N allowed wave vectors in the first Brillouin zone, and $\sigma=1,...,4$ labels one of the four Davydov components. Furthermore, $\phi_{\sigma s}(\mathbf{q})$ is the sth element of the σth normalized eigenvector of the 4×4 reduced Hamiltonian,

$$H_{s,s'}(\mathbf{q})=\epsilon\delta_{s,s'}+\sum_{\mathbf{n}}{}'\ L_{s,s'}(\mathbf{n})e^{-i\mathbf{q}\cdot\mathbf{n}}, \tag{5}$$

with corresponding eigenvalues $E_{\mathbf{q}\sigma}$. The state $|\mathbf{q}\sigma\rangle$ is a one-quantum eigenstate with energy $E_{\mathbf{q}\sigma}$. Because of the translational symmetry of the system, only transitions to states with $\mathbf{q}=\mathbf{0}$ are dipole-allowed from the ground state, with a dipole given by $\boldsymbol{\mu}_{0\sigma}=\sqrt{N}\Sigma_s\phi^*_{\sigma s}(\mathbf{0})\boldsymbol{\mu}_s\equiv\sqrt{N}\boldsymbol{\mu}_\sigma$ (* denoting the complex conjugate).[45] The method described here can equally well be applied to parallel β sheets, which contain only two oscillators per unit cell ($s=1,2$).

Imposing periodic boundary conditions reduces the effort to calculate the one-quantum states to a small (4×4) diagonalization for every wave vector $\mathbf{q}$. With these boundary conditions, the calculation of the two-quantum states also simplifies, as they may be separated into decoupled states with different center-of-mass wave vector. We will not give explicit expressions here, as for a translationally invariant system with periodic boundary conditions it is even possible to calculate two-dimensional spectra without explicit calculation of the two-quantum states (cf. Sec. III C).

III. EXPRESSIONS FOR THE SPECTRA

A. Linear spectrum

The infrared absorption spectrum, also referred to as the linear spectrum, is given by

$$I(\omega) = -\,\mathrm{Im}\sum_b \frac{|\boldsymbol{\mu}_b|^2}{\omega - E_b + i\gamma}, \tag{6}$$

where the summation extends over all one-quantum eigenstates, formally denoted by $|b\rangle$, and we have set $\hbar=1$. The Lorentzian line shape invoked in Eq. (6) assumes that the homogeneous limit applies. Although for real proteins the dephasing dynamics are much more complicated, considering this limit is still instructive. Except when indicated otherwise, we will set $\gamma = 8\ \mathrm{cm}^{-1}$, which, in order to allow a better distinction of spectral features in our model, has been chosen somewhat smaller than measured dephasing rates of peptides and proteins.[7,22–24,49] In the linear spectrum, a Lorentzian absorption peak occurs for each dipole-allowed one-quantum state, centered at its transition energy and with an area proportional to its squared dipole moment. In the special case where we assume periodic boundary conditions, the summation over b in Eq. (6) collapses to a sum over four terms (two for the parallel sheet), corresponding to the $\mathbf{q}=\mathbf{0}$ states of the four Davydov bands $\sigma=1,...,4$ [cf. Eq. (4)].

B. Two-dimensional spectrum: Brute-force method

In Fourier-transform 2DIR spectroscopy, three, femtosecond pulses, each with a unique wave vector, k_i $(i=1,2,3)$, are incident on the sample. The short pulses have sufficient bandwidth that they are resonant both with the fundamental $(v=0\rightarrow1)$ transition, as well as the transitions between the singly and doubly excited states $(v=1\rightarrow2)$, that is $\omega\approx\epsilon$ and $\epsilon-A$. These pulses sequentially drive absorption and stimulated emission processes between these three levels. After each field, the system evolves freely under the model Hamiltonian [Eq. (1)], during three sequential time periods t_i. After the three interactions, an induced third-order nonlinear polarization P radiates a nonlinear signal during t_3, into a wave-vector matched direction k_s. In practice, we then heterodyne detect the signal to measure the amplitude and phase of the nonlinear response of the system. Through a Fourier transform, the 2DIR spectrum correlates the coherent evolution of the system during t_1 and t_3.

We calculate the 2DIR correlation spectrum using the third-order nonlinear response function S represented by the six Feynman diagrams shown in Fig. 3. Two types of signals,

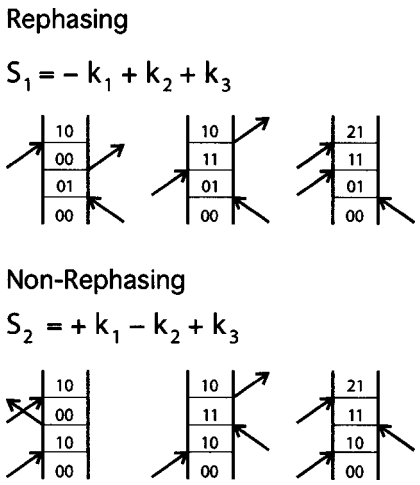

FIG. 3. Feynman diagrams for the 2DIR signals S_1 and S_2. 0 represents the ground state of the system, 1 a general one-quantum excited state, and 2 a general two-quantum excited state. The 2DIR correlation spectrum is the sum of the negative of the imaginary parts of the frequency domain signals S_1 and S_2.

S_1 (rephasing) and S_2 (nonrephasing), sum to give the correlation spectrum. The rephasing signal S_1 is a photon-echo pulse sequence with the phase matching condition, $\mathbf{k}_s = -\mathbf{k}_1+\mathbf{k}_2+\mathbf{k}_3$ in which the coherences evolve during t_1 and t_3 with conjugate phase. The nonrephasing signal S_2 scatters into the $\mathbf{k}_s=+\mathbf{k}_1-\mathbf{k}_2+\mathbf{k}_3$ phase matching direction, resulting in coherences during t_1 and t_3 that evolve with the same phase. For the purpose of calculating signals, we assume short, well-separated pulses with the appropriate time ordering for each of the signal pathways, so that the expression for the radiated signal is proportional to the nonlinear response function. The effects of finite duration pulses (not considered here) can be treated by applying standard convolution methods to the response functions.[51] The signals in the frequency domain can be expressed through a two-dimensional complex Fourier transform of the time-domain response:

$$S_n(\omega_1,t_2,\omega_3) = -\,\mathrm{Im}\left[\int_0^\infty dt_1\int_0^\infty dt_3 S_n(t_1,t_2,t_3)e^{\pm i\omega_1 t_1 + i\omega_3 t_3}\right]. \tag{7}$$

In this expression, we use $e^{-i\omega_1 t_1}$ for S_1 and $e^{+i\omega_1 t_1}$ for S_2, so that the frequency domain representations of the spectra appear with resonances in the positive ω_1 and ω_3 quadrant for both signals.[5] The correlation spectrum that we plot is $S_c=S_1+S_2$ which has simple absorptive line shapes and eliminates the phase twisted behavior present in each of the constituent spectra.[5,52,53] For $t_2=0$ there is an additional contribution to the signal commonly referred to as S_3 that shows exactly the same features as S_2.[5,52,53] We have calculated the S_3 response for our model to confirm that it has no significant impact on the calculated spectra, but, to simplify the computation, we neglect this contribution for all of the data presented here.

We calculate the response function for these diagrams in the frequency domain with Lorentzian line shapes in both frequencies ω_1 and ω_3. In each of the diagrams, the first two

interactions involve only the ground and first excited vibrational states of the system. These interactions require two independent summations over the one-quantum eigenstates. The third interaction can involve either the one-quantum states (first two diagrams of S_1 and S_2) or the two-quantum states (the third diagrams). The expressions for S_1 and S_2 are easily derived using the standard rules for third-order nonlinear response functions[51,54] giving the expressions

$$S_1(\omega_1,t_2,\omega_3) = -\mathrm{Im}\sum_{d,b}\left\{\boldsymbol{\mu}_d^*\boldsymbol{\mu}_d\boldsymbol{\mu}_b\boldsymbol{\mu}_b^*\frac{i}{-\omega_1+E_d+i\gamma}\frac{1}{\omega_3-E_b+i\gamma} + \boldsymbol{\mu}_d^*\boldsymbol{\mu}_b\boldsymbol{\mu}_d\boldsymbol{\mu}_b^*\frac{i}{-\omega_1+E_d+i\gamma}\frac{1}{\omega_3-E_b+i\gamma}e^{iE_{db}t_2} + \sum_c \boldsymbol{\mu}_d^*\boldsymbol{\mu}_b\boldsymbol{\mu}_{cb}\boldsymbol{\mu}_{cd}^*\frac{-i}{-\omega_1+E_d+i\gamma}\frac{1}{\omega_3-E_{cd}+i\gamma} \times e^{iE_{db}t_2}\right\} \tag{8}$$

and

$$S_2(\omega_1,t_2,\omega_3) = -\mathrm{Im}\sum_{d,b}\left\{\boldsymbol{\mu}_d\boldsymbol{\mu}_d^*\boldsymbol{\mu}_b\boldsymbol{\mu}_b^*\frac{i}{\omega_1-E_d+i\gamma}\frac{1}{\omega_3-E_b+i\gamma} + \boldsymbol{\mu}_d\boldsymbol{\mu}_b^*\boldsymbol{\mu}_b\boldsymbol{\mu}_d^*\frac{i}{\omega_1-E_d+i\gamma}\frac{1}{\omega_3-E_d+i\gamma}e^{-iE_{db}t_2} + \sum_c \boldsymbol{\mu}_d\boldsymbol{\mu}_b^*\boldsymbol{\mu}_{cd}\boldsymbol{\mu}_{cb}^*\frac{-i}{\omega_1-E_d+i\gamma}\frac{1}{\omega_3-E_{cb}+i\gamma} \times e^{-iE_{db}t_2}\right\}. \tag{9}$$

Here, the summations over d and b run over all one-quantum states and the one over c extends over all two-quantum states. Furthermore, we defined $E_{db}\equiv E_d-E_b$, $E_{cd}\equiv E_c-E_d$, and $E_{cb}\equiv E_c-E_b$. For our calculations we set $t_2=0$. We calculate 2DIR spectra for the *ZZYY* polarization condition, in which the first and second field are polarized perpendicularly to the third field, using the approach published elsewhere.[5,13,54]

The 2DIR correlation spectrum in general contains positive peaks, which derive from stimulated emission and bleaching of the one-quantum states, and negative peaks, associated with induced absorption transitions from the one-quantum states to the two-quantum states. The positive peaks appear on the diagonal of the spectrum $\omega_1=\omega_3=E_d$, and also as cross peaks between one-quantum resonances [$\omega_1=E_d,\omega_3=E_b$ $(b\neq d)$]. These cross peaks are interesting, because their intensity is the product of the squared dipoles of two different one-quantum states, implying that weak transitions which are invisible in the linear spectrum, may show up as a cross peak with a strong transition in the 2DIR spectrum. Associated with each positive peak are negative induced absorption peaks, shifted to lower frequency in ω_3. This redshift relative to the one-quantum resonances results from the anharmonic nature of the oscillators. If we let A tend to zero, the redshift vanishes, and positive and negative peaks overlap, leading to a vanishing net 2DIR spectrum. The physical reason is that the sheet then represents a collection of purely harmonic oscillators, which exhibit no nonlinear response. More details will be discussed in Sec. V.

C. Two-dimensional spectrum: Scattering approach

As explained already in Sec. II B, the brute force evaluation of Eqs. (8) and (9) quickly becomes numerically demanding with increasing sheet size. For our model, however, it is not necessary to explicitly calculate and perform the sum over the two-quantum states. The reason is that the anharmonic term in the Hamiltonian Eq. (1) only applies to double excitations on one oscillator (overtones). The Green function for the two-particle states in the presence of such an on-site interaction can be expressed exactly in terms of the one-quantum states and energies.[42–45] The 2DIR spectrum can be expressed in terms this Green function resulting in a simpler method to calculate the spectrum. Although the method may be applied to systems with disorder and open boundary conditions, we will use it only for the simplest case, where we neglect disorder (as we have all along) and impose periodic boundary conditions.

Below we present the expressions for the diagrams S_1 and S_2 obtained using this scattering method. They have been derived by closely following the derivation of the electronic pump-probe spectrum for Frenkel exciton systems by Juzeliūnas and Knoester.[45] The main difference from the previous derivation is that in Frenkel exciton systems the anharmonicity tends to infinity, i.e., two electronic excitation quanta are not allowed to occupy the same site. The second difference is that the Feynman diagrams that we consider here involve a slightly richer variety of Green-function matrix elements than the pump-probe spectrum. Both differences can be accounted for in a straightforward way.

In order to make a connection to the work of Juzeliūnas and Knoester,[45] we reconsider Eq. (8) for S_1. The summations over the one-particle states are straightforward (especially if we impose periodic boundary conditions, due to the selection rule $\mathbf{q}=\mathbf{0}$). The complicating part of the expression is the quantity

$$R=\sum_c \boldsymbol{\mu}_{cb}\boldsymbol{\mu}_{cd}^*\frac{1}{\omega_3-E_{cd}+i\gamma}, \tag{10}$$

which may be rewritten as

$$R=\langle d|\mathbf{M}_-G(\omega_3+E_d)\mathbf{M}_+|b\rangle, \tag{11}$$

where $\mathbf{M}_-=\mathbf{M}_+^\dagger$ is the sheet's dipole operator associated with removing one vibrational quantum, and $G(\omega)=(\omega-H+i\gamma)^{-1}$ denotes the Green function of the sheet. The expression in Eq. (11) is of the same form as those considered in Ref. 45, except that for the pump-probe spectrum, only diagonal matrix elements $(d=b)$ are involved. Including the nondiagonal elements does not lead to a major complication in the derivation. The Green function in R may be restricted to the two-quantum subspace of the sheet, as is clear from the fact that the operator $\mathbf{M}_+$ acting to the right

generates a two-quantum state. The crux of the method is now that the two-particle Green operator of the system with the on-site anharmonicity may be expressed in terms of the Green operator G_0 in the absence of the anharmonicity. One obtains[45]

$$G = G_0 - AG_0Q(Q + AQG_0Q)^{-1}QG_0, \tag{12}$$

where the operator Q projects out overtone states of the original site basis: $Q = (1/2)\Sigma_{\mathbf{ns}} a^{\dagger}_{\mathbf{ns}} a^{\dagger}_{\mathbf{ns}} a_{\mathbf{ns}} a_{\mathbf{ns}}$. For the case of Frenkel excitons, also referred to as hard-core bosons, one now takes the limit $A \to \infty$, which leaves the expression $G_{\mathrm{hcb}} = G_0 - G_0(QG_0Q)^{-1}G_0$.[45] Keeping a finite value for A is, however, no complication in the method. G_0 refers to the system without anharmonicity and is easily expressed in terms of the one-quantum eigenstates, so that, using Eq. (12), R (and its analog in S_2) may be expressed in terms of one-quantum eigenstates. The remaining steps may be worked out in direct analogy to Ref. 45, and, without giving more details, we directly present the final results for the Feynman diagrams:

$$S_1(\omega_1, t_2, \omega_3) = -\mathrm{Im}\, 2AN \sum_{\sigma,\sigma',\sigma'',\sigma'''} \boldsymbol{\mu}^*_{\sigma} \boldsymbol{\mu}_{\sigma'} \boldsymbol{\mu}_{\sigma''} \boldsymbol{\mu}^*_{\sigma'''} \times \frac{i e^{-i(E_{0\sigma'} - E_{0\sigma})t_2}}{-\omega_1 + E_{0\sigma} + i\gamma} \sum_{s,s'} g_{s'}(\sigma, \sigma', \sigma'') F^{-1}_{s,s'} f_s(\sigma, \sigma''') \tag{13}$$

and

$$S_2(\omega_1, t_2, \omega_3) = -\mathrm{Im}\, 2AN \sum_{\sigma,\sigma',\sigma'',\sigma'''} \boldsymbol{\mu}_{\sigma'} \boldsymbol{\mu}^*_{\sigma} \boldsymbol{\mu}_{\sigma''} \boldsymbol{\mu}^*_{\sigma'''} \times \frac{i e^{-i(E_{0\sigma'} - E_{0\sigma})t_2}}{\omega_1 - E_{0\sigma'} + i\gamma} \times \sum_{s,s'} g_{s'}(\sigma, \sigma', \sigma'') F^{-1}_{s,s'}(\sigma) f_s(\sigma, \sigma'''). \tag{14}$$

Here, the dipoles $\boldsymbol{\mu}_{\sigma}$ are as defined below Eq. (5). Furthermore we defined

$$g_{s'}(\sigma, \sigma', \sigma'') = \frac{\phi_{\sigma' s'}(\mathbf{0}) \phi_{\sigma'' s'}(\mathbf{0})}{\omega_3 + E_{0\sigma} - E_{0\sigma'} - E_{0\sigma''} + i\gamma}, \tag{15}$$

and

$$f_s(\sigma, \sigma''') = \frac{\phi^*_{\sigma s}(\mathbf{0}) \phi^*_{\sigma''' s}(\mathbf{0})}{\omega_3 - E_{0\sigma'''} + i\gamma}. \tag{16}$$

Finally, $F^{-1}_{s,s'}(\sigma)$ is the s, s' element of the inverse of the 4×4 scattering matrix $F_{s,s'}(\sigma)$ defined through

$$F_{s,s'}(\sigma) = \delta_{s,s'} + \frac{A}{N} \sum_{\mathbf{q},\sigma_1,\sigma_2} \times \frac{\phi_{\sigma_1 s}(\mathbf{q}) \phi_{\sigma_2 s}(-\mathbf{q}) \phi^*_{\sigma_1 s'}(\mathbf{q}) \phi^*_{\sigma_2 s'}(-\mathbf{q})}{\omega_3 + E_{0\sigma} - E_{\mathbf{q}\sigma_1} - E_{-\mathbf{q}\sigma_2} + i\gamma}. \tag{17}$$

In all these expressions, $\phi_{\sigma s}(\mathbf{q})$ refer to the eigenvector components of the reduced one-quantum Hamiltonian defined below Eq. (4). The summation over $\mathbf{q}$ in Eq. (17) extends over the entire first Brillouin zone. Explicitly, for the $N_x \times N_y$ sheet we have $\mathbf{q} = (q_x, q_y)$, with $q_i = (2\pi l_i / N_i)$ $(i = x, y)$, where $l_i = 0, \pm 1, \pm 2, \ldots, \pm(N_i/2 - 1), N_i/2$ (if $N_i =$ even) and $l_i = 0, \pm 1, \pm 2, \ldots, \pm(N_i - 1)/2$ (if $N_i =$ odd).

Although the scattering method to calculating the 2DIR spectra is more complex than the brute-force method, its numerical advantage is easily perceived. In the brute-force approach the nested summations over states in Eqs. (8) and (9) cause the calculation time to scale as $N^4 = (SN_xN_y)^4$ (for an arbitrary number of oscillators S per unit cell). Using Eqs. (13) and (14) of the scattering method, the calculation only scales as $S^6 N_x N_y$. As an example, consider the antiparallel sheet with $N_x = N_y = 5$, leading to $N = 100$ $(S = 4)$. For this system, the brute-force approach takes 1000 times longer than the calculation via the scattering approach. Of course, we should keep in mind that this only holds in the case of an ordered sheet with periodic boundary conditions. For more general conditions, the scattering method may still be used, but the advantage is reduced, because the calculation of the Green function requires the inversion of $N \times N$ scattering matrices. We note that the scattering method also has a conceptual advantage,[42] as it focuses directly on the source of the nonlinearity, namely the scattering resulting from the anharmonic nature of the oscillators. This is explicitly visible from the fact that the signals S_1 and S_2 in Eqs. (13) and (14), respectively, vanish identically for $A = 0$.

This approach is general and does not depend on the assumption of short, separated pulses. As before, finite pulse duration effects could be accounted for using standard convolution methods for the response functions though now it must be noted that the response function calculated in this way is represented in the frequency domain with respect to the first and third evolution periods and the appropriate frequency domain convolution would have to be applied or else the response function would have to be transformed into the time domain thus complicating the calculation of the signal for finite duration pulses. We finally note that, as for the brute-force method, we calculate the orientational response for the four transition dipole moments in Eqs. (13) and (14) ignoring orientational relaxation.

IV. ANALYTICAL AND NUMERICAL ONE-QUANTUM EIGENSTATES

To better understand the results we present in Sec. V, it is useful to have a basic understanding of the nature of the one-quantum eigenstates. To this end, we derive analytical expressions for these states. Because of the symmetry of the Hamiltonian the expressions are straightforward for the case of periodic boundary conditions. We also demonstrate that for the hairpin the important one-quantum states can be determined to a very good approximation without imposing periodic boundary conditions. The analytical results agree well with numerically exact ones.

TABLE II. Energies, transition dipole vectors, and squared magnitudes of the transition dipole vectors for each of the eigenstates of the single unit cell. Energies are given in wave numbers and dipole vectors are represented in Cartesian coordinates.

State	Energy (cm^{-1})	Dipole (μ)	Dipole^2 (μ^2)
$s+$	1696	$-0.22\hat{z}$	0.05
$s-$	1674	$-0.13\hat{z}$	0.017
$a+$	1677	$0.51\hat{x}+0.75\hat{y}$	0.82
$a-$	1653	$-0.23\hat{x}+1.75\hat{y}$	3.1

A. Single unit cell

Although the single unit cell of the antiparallel sheet does not correspond to a physically meaningful realization, it is useful to study this case as a basis for hairpins and extended sheets. As is clear from Fig. 2, the one-quantum Hamiltonian has C_2 symmetry about the center of the unit cell, i.e., it is symmetric under the simultaneous interchange of the oscillators 1 and 4 and oscillators 2 and 3. This suggests choosing a new basis consisting of the symmetric states $|s_{32}\rangle=(1/\sqrt{2})(|3\rangle+|2\rangle)$ and $|s_{14}\rangle=(1/\sqrt{2})(|1\rangle+|4\rangle)$ and the antisymmetric states $|a_{32}\rangle=(1/\sqrt{2})(|3\rangle-|2\rangle)$ and $|a_{14}\rangle=(1/\sqrt{2})(|1\rangle-|4\rangle)$. Here $|s\rangle$ $(s=1,...,4)$ denotes the basis state in which oscillator s has one vibrational quantum and the others are in the ground state. In this new basis, the two symmetric states are decoupled from the two antisymmetric ones, and the one-quantum Hamiltonian takes the explicit form

$$H_{\text{cell}}=\begin{pmatrix} \epsilon+L_4 & L_2+L_5 & 0 & 0 \\ L_2+L_5 & \epsilon+L_1 & 0 & 0 \\ 0 & 0 & \epsilon-L_4 & L_2-L_5 \\ 0 & 0 & L_2-L_5 & \epsilon-L_1 \end{pmatrix}. \tag{18}$$

The 2×2 block matrices are easily diagonalized. The symmetric eigenstates are

$$|s\pm\rangle=\cos\varphi_{s\pm}|s_{32}\rangle+\sin\varphi_{s\pm}|s_{14}\rangle, \tag{19}$$

where $\tan\varphi_{s\pm}=r_s\pm\text{sgn}(L_2+L_5)\sqrt{1+r_s^2}$, with $r_s=(L_1-L_4)/2(L_2+L_5)$, and the associated eigenenergies are

$$E_{s\pm}=\epsilon+\frac{L_1+L_4}{2}\pm\sqrt{\left(\frac{L_1-L_4}{2}\right)^2+(L_2+L_5)^2}. \tag{20}$$

The antisymmetric states are

$$|a\pm\rangle=\cos\varphi_{a\pm}|a_{32}\rangle+\sin\varphi_{a\pm}|a_{14}\rangle, \tag{21}$$

with $\tan\varphi_{a\pm}=r_a\pm\text{sgn}(L_2-L_5)\sqrt{1+r_a^2}$, with $r_a=(L_4-L_1)/2(L_2-L_5)$ and

$$E_{a\pm}=\epsilon-\frac{L_1+L_4}{2}\pm\sqrt{\left(\frac{L_1-L_4}{2}\right)^2+(L_2-L_5)^2}. \tag{22}$$

Using the coupling constants given in Fig. 2 and the dipole orientations of Table I, these expressions give the transition energies and the transition dipole vectors and magnitudes shown in Table II. Clearly, the antisymmetric states dominate the absorption spectrum; they are both polarized in the plane of the sheet, and the angle between their transition moments is 41°. The strongest state ($|a-\rangle$) is redshifted relative to the single-oscillator transition ϵ by about 20 cm^{-1}, while the second strongest state ($|a+\rangle$) almost coincides with ϵ. The other two transitions are polarized perpendicular to the sheet and are almost completely dark. We stress that these are exact solutions to the unit-cell problem. The nature of the solutions is dictated by the symmetry of the system and not by the precise nature or magnitude of the interactions. Within the transition dipole coupling model, the energy splittings are proportional to the value for C in Eq. (2), but both the orientation and magnitude of the eigenstate transition dipole vectors are independent of this constant.

It is interesting to note that there is a similarity between the eigenstates of the unit cell and the states found by Miyazawa for the amide I vibrational spectrum of infinite β sheets with periodic boundary conditions.[34,35] Miyazawa identifies four states with the eigenvectors,

$$\begin{aligned} |(0,0)\rangle&=\tfrac{1}{2}(|1\rangle+|2\rangle+|3\rangle+|4\rangle),\\ |(\pi,0)\rangle&=\tfrac{1}{2}(-|1\rangle+|2\rangle-|3\rangle+|4\rangle),\\ |(0,\pi)\rangle&=\tfrac{1}{2}(|1\rangle+|2\rangle-|3\rangle-|4\rangle),\\ |(\pi,\pi)\rangle&=\tfrac{1}{2}(-|1\rangle+|2\rangle+|3\rangle-|4\rangle). \end{aligned} \tag{23}$$

The correspondence between these states and the cell states can be seen by considering the phases. For $|(0,0)\rangle$ and $|(\pi,\pi)\rangle$ oscillators 1 and 4 are in phase, which is also the case for our s states. For $|(\pi,0)\rangle$ and $|(0,\pi)\rangle$ they are in antiphase, which agrees with our a states. To distinguish within these two classes, we have to look at the relative phases of oscillators 1 and 3, to which end we have to consider the angles $\phi_{s\pm}$ and $\phi_{a\pm}$. We then find that Miyazawa's $|(0,0)\rangle$ state is analogous to our $|s-\rangle$ state, his $|(\pi,0)\rangle$ state is analogous to our $|a-\rangle$ state, his $|(0,\pi)\rangle$ state is analogous to our $|a+\rangle$ state, and his $|(\pi,\pi)\rangle$ state is analogous to our $|s+\rangle$ state.

B. Hairpins

For hairpins, it is straightforward to obtain analytical solutions for the one-quantum states by imposing periodic boundary conditions. The effective 4×4 Hamiltonian of Eq. (5) has the same symmetry properties as the Hamiltonian of the single unit cell and may thus be diagonalized using the same methods. The results depend on the range of interactions taken into account between different cells and therefore, in principle, also depend on the length N_x of the hairpin. However, as is clear from Fig. 2, even the dominant intercell interactions are weak and one expects that the results quickly converge with increasing N_x. Without giving details, we assert that for $\mathbf{q}=\mathbf{0}$ (the class of states visible in absorption), and taking into account only the interactions given in Fig. 2, the optically dominant states are the antisymmetric ones, with energies and squared dipoles given by $E_{a-}=1656\ cm^{-1}$, $\mu_{a-}^2=3.34\ \mu^2$ and $E_{a+}=1677\ cm^{-1}$, $\mu_{a+}^2=0.58\ \mu^2$. The transition moments of these states lie in the plane of the sheet, with an angle of 49° between them. Comparing these numbers to Table II, we notice that in the hairpin the intercell interactions, owing to their small size, have only small effects on the eigenstates.

Due to the small range and size of the intercell interactions in the hairpin, it is possible to obtain analytical results that properly account for finite-size effects, i.e., in which we do not impose periodic boundary conditions. This calculation is of interest, as it allows for an analytical understanding of size effects on the spectra. We briefly outline the method. We start from the $4N_x$-dimensional basis consisting of the four eigenstates of each of the N_x isolated unit cells. These states are coupled to each other by the intercell interactions. We should distinguish the couplings between cell states of the same type (e.g., all states $|a-_n\rangle$, with $n=1,...,N_x$) from those between different types. As states of the same type are degenerate, their coupling should be accounted for, no matter how small it is. The coupling between different types of states, however, needs to be accounted for only if it is comparable to or larger than the splitting between the energies of these cell states. The electrostatic couplings fall off rapidly with distance, and only interactions between neighboring cells are important, so the problem of coupling cell states of one type reduces to the standard problem of one particle hopping on an open chain with nearest-neighbor interactions. The resulting antisymmetric (optically dominant) states are

$$|a\pm_k\rangle = \sqrt{\frac{2}{N_x+1}} \sum_{n=1}^{N_x} \sin\left(\frac{\pi k n}{N_x+1}\right) |a\pm_n\rangle, \tag{24}$$

with energies

$$E_{a\pm}(k) = E_{a\pm} + 2J^a_{\pm} \cos\left(\frac{\pi k}{N_x+1}\right). \tag{25}$$

Here, $k=1,2,...,N_x$ and the constants $J^a_{\pm}$ are given by $J^a_+ = \langle a+_n|H|a+_{n+1}\rangle = 1.4\ \mathrm{cm}^{-1}$ and $J^a_- = \langle a-_n|H|a-_{n+1}\rangle = 2.7\ \mathrm{cm}^{-1}$. Similar expressions, with similarly small dispersion constants $J^s_{\pm}$ may be derived for the two bands resulting from the symmetric basis states. We have checked that the coupling matrix elements between cell states of different type are all smaller in magnitude than 2 cm^{-1}. With reference to the energies in Table I, this implies that the mixing between different types of states is weak and Eq. (24) and its analog for the symmetric states give accurate expressions for the eigenstates of the finite hairpin.

One easily shows that within each band the state with quantum label $k=1$ takes almost all oscillator strength: $\geqslant 81\%$ of the band's total, with the $k=3$ state taking roughly 9%.[55] As a consequence, the three states $|a-_{k=1}\rangle$ (with squared dipole moment $2.5N_x\mu^2$), $|a-_{k=3}\rangle$ ($0.28N_x\mu^2$), and $|a+_{k=1}\rangle$ ($0.66N_x\mu^2$) dominate the absorption spectrum of the hairpin. The energies of these states gradually shift from the single-cell energies given in Table I to the values $E_{a\pm}+2J^a_{\pm}$ in the limit of large N_x, with the $k=3$ state having lower energy than the $k=1$ state. The transition dipole vector orientations are the same as those of the cell states, as the above states do not account for mixing of different cell states. If we account for this mixing between the dominant states $|a-_{k=1}\rangle$ and $|a+_{k=1}\rangle$ by using first-order perturbation theory, the angle between the dipoles of these states is found to change from 41° for $N_x=1$ (single cell) to 49° (N_x large) and the ratio of their squared dipole moments increases from 3.8 to 5.5. We note that in the limit of large N_x all the results derived here tend to those obtained for periodic boundary conditions, as should be the case. However, the advantage of Eqs. (24) and (25) (with first-order mixing) is that they properly interpolate between $N_x=1$ and $N_x\to\infty$.

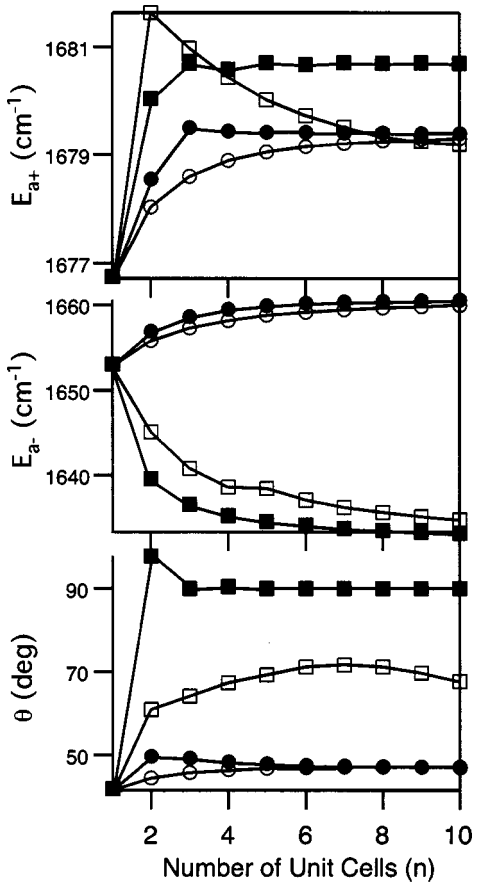

FIG. 4. Plots of the energy of the states corresponding to $a+$ (top) and $a-$ (middle) and the angle between the transition dipole vectors of those states (bottom) versus the number of unit cells. Squares refer to extended sheets ($N_x\times N_y$ with $N_x=N_y$) and circles refer to hairpins ($N_x\times 1$). The filled markers are for calculations assuming periodic boundary conditions and the open markers are for systems with open boundary conditions.

The analytical results derived here compare very well to the exact ones obtained numerically and accounting for all interactions in the hairpin. The numerical results show two dominant infrared transitions. The energies of these transitions and the angle between their dipoles are plotted in Fig. 4 as a function of the length N_x of the hairpin. Closed circles are the numerical results for periodic boundary conditions and open are those for open boundary conditions, which account for edge effects. The squares are the same data for extended sheets and will be discussed in Sec. IV C. The upper panel displays the energy of the higher-energy (weaker) transition, associated with the $|a+\rangle$ state; the middle panel does the same for the lower-energy (stronger) transition, associated with $|a-\rangle$, and the bottom panel gives the angle between these two transitions. We first note that for $N_x=1$, the single-cell results of Table II are, of course, recovered. With increasing N_x, both peaks shift to higher energy, in accordance with the positive dispersion parameter $J^a_{\pm}$ introduced above. In the language of molecular aggregates, these states belong to H (hypsochromatic) bands. The small nu-

merical values of the blueshifts also agree rather well with the above analytical estimates of 2.8 and 5.4 cm^{-1}, respectively. This small energy dispersion is a direct result of the weak and short-range intercell interactions, which also explain why the results for periodic and open boundary conditions do not differ very much. This behavior also holds for the angle between the dipoles of the two dominant states, which is seen to exhibit a very small size dependence and agrees well with the analytical results. Both dipoles indeed lie in the plane of the sheet, with the $a-$ dipole always very close to the Y axis.

For open boundary conditions, our numerical results indeed show satellite states of each of the main peaks, associated with weaker transitions in each of the bands (cf. the $k=3$ states mentioned above). We finally mention that numerical calculations also find a very weak transition around 1700 cm^{-1} associated with the $|s+\rangle$ state having a small negative energy dispersion of about 1 cm^{-1}.

C. Extended sheets

As for hairpins, it is straightforward to obtain analytical solutions for the one-quantum states of extended sheets by imposing periodic boundary conditions. Again, the effective 4×4 Hamiltonian of Eq. (5) maintains the symmetry properties of the Hamiltonian of the unit cell, so that the same diagonalization procedure may be used. A difference with the hairpin is that the additional interactions introduced by adding more rows in the sheet are much larger (cf. Fig. 2). Without giving details, we assert that for $\mathbf{q}=\mathbf{0}$ and taking into account only the interactions given in Fig. 2, the optically dominant states are again the antisymmetric ones, with energies and squared dipoles given by $E_{a-}=1644\ cm^{-1}$, $\mu^2_{a-}=3.81\ \mu^2$ and $E_{a+}=1677\ cm^{-1}$, $\mu^2_{a+}=0.32\ \mu^2$. The dipole directions are practically along the Y (X) axis for $|a-\rangle$ ($|a+\rangle$), i.e., essentially perpendicular to each other. The strong interactions between cells in different rows cause larger deviations from the unit-cell eigenstates as compared to the hairpin. Because the interrow interactions are stronger than the energy separations between the different single-cell eigenstates, it is, in contrast to the case of the hairpin, impossible to find simple analytical solutions that account for finite-size effects. We note that due to the strong mixing of the cell eigenstates, strictly speaking, the labels $a-$, $a+$, $s-$, and $s+$ cannot be used to distinguish various classes of eigenstates of the extended sheet. The use of these labels now acquires a looser meaning of referring to the relative in-phase and out-of phase behavior of the four oscillators in the unit cell.

We have studied finite extended sheets (open boundary conditions) including all interactions using numerical diagonalization. The results for the two dominant transitions are displayed in Fig. 4 for square ($N_x\times N_x$) sheets. Similar to the hairpin, open (closed) squares refer to open (periodic) boundary conditions. We first notice that for the extended systems the $a+$ state again exhibits a blueshift with increasing size (H band), while the $a-$ state shifts to the red (J band). This is in agreement with the analytical results; the values of the analytical and numerical shifts do not agree as well as in the case of the hairpin, as the two-dimensional nature of the sheet makes the solutions more sensitive to long-range interactions. In addition, the interrow interactions in extended sheets are rather strong, which causes a much stronger size dependence of the energies and angle between the dipoles than in the case of the hairpin. As we see from the figure, the angle between the dipoles still differs appreciably for the two types of boundary conditions for sheets with 10×10 unit cells. Only at very large (physically not meaningful) sizes does one find agreement.

Finally, as for the hairpin, one numerically finds weaker satellite peaks of the dominant transitions in the case of open boundary conditions. We also see the weak transition around 1700 cm^{-1} polarized perpendicularly to the sheet, associated with the $|s+\rangle$ state.

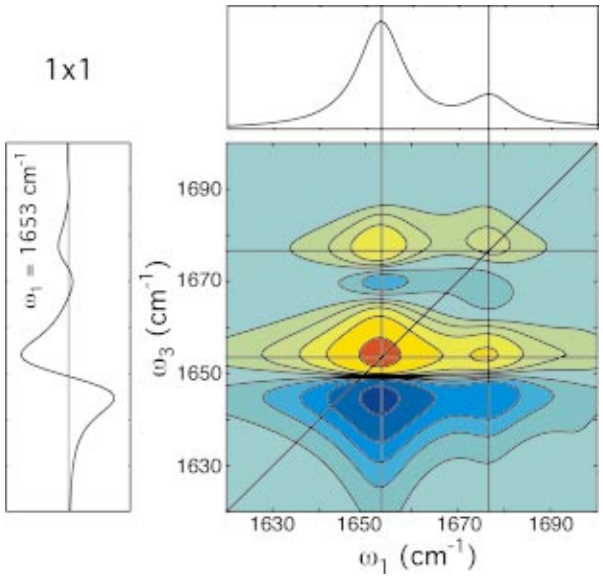

FIG. 5. (Color) Linear absorption spectrum (top) 2DIR spectrum (*ZZYY*) calculated with periodic boundary conditions (center) and a slice from the 2DIR spectrum with $\omega_1=1653\ cm^{-1}$ corresponding to the transition energy for going to the dominant $a-$ state for a single unit cell (1×1). There are lines drawn on the 2D plot in both ω_1 and ω_3 at the frequencies of the two strongest transitions $a-$ and $a+$, and there is also a line indicating the diagonal, $\omega_1=\omega_3$. The contours are drawn cutting off the tops of the strong diagonal peaks to emphasize the cross peaks. Red peaks are positive and blue peaks are negative.

V. SPECTRA: RESULTS AND DISCUSSION

We have calculated the linear and 2DIR spectra of antiparallel β sheets for various shapes and sizes. In Figures 5–7 we show the results for the case of one unit cell (1×1 system), a hairpin of seven unit cells (7×1), and an extended square sheet of 49 unit cells (7×7), respectively. The latter two systems employ periodic boundary conditions, and we calculate the 2DIR spectra using Eqs. (13) and (14). Each figure shows the linear absorption spectrum at the top, the 2DIR spectrum for the *ZZYY* polarization condition, and a slice from the two-dimensional spectrum for constant ω_1 at the frequency of the largest transition in the linear spectrum, corresponding to the state $|a-\rangle$. In the 2DIR spectra, we have drawn the contours to cut off the tops of the diagonal peaks and highlight the smaller cross peaks. The blue peaks

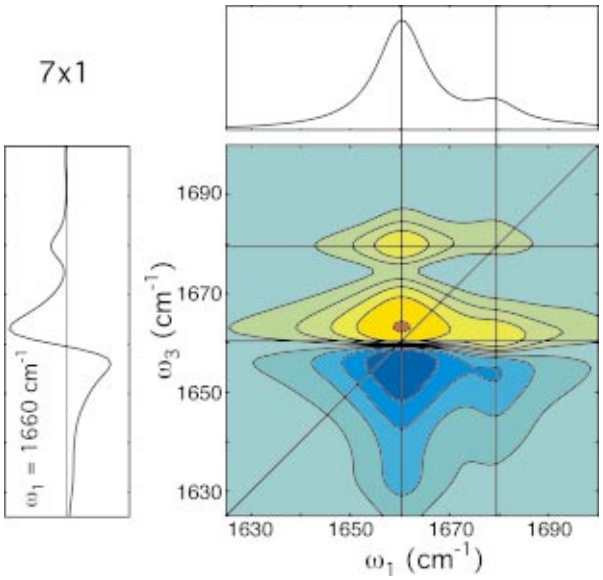

FIG. 6. (Color) Linear and 2DIR spectra as in Fig. 5 but for a 7×1 hairpin with the slice taken along $\omega_1=1660\ \mathrm{cm}^{-1}$.

in the contour plots have negative intensity, while the yellow/red peaks are positive. We choose the *ZZYY* polarization condition for the spectra because, for the typical angles between transition dipoles in this system, that polarization condition has the largest cross peak amplitude relative to the diagonal transitions.

As expected, the linear spectra all show two main features, corresponding to the $a-$ and $a+$ bands. Clearly, the former peak is by far the strongest, in agreement with our analytical estimates in Sec. IV. The weak $s+$ band only stands out in the 7×7 spectrum, though it is present in all cases. For the two-dimensional spectra, in addition to the positive diagonal peaks of the strong transitions, we clearly see the positive cross peaks between the $a-$ and $a+$ states, and in the 7×7 system we even see the cross peak of $a-$ and $s+$. This feature underlines one advantage of two-dimensional spectroscopy, mentioned in Sec. III B, the ability to identify weak transitions. As we expect, the cross peaks of $a-$ and $a+$ have a larger intensity than the diagonal peak of $a+$. The cross peaks are most clearly seen in the $\omega_1=$constant slices in each figure. Because cross peaks are removed from the spectral congestion along the diagonal, they are more reliable structural markers. A second advantage of two-dimensional spectroscopy is that the intensity of the cross peaks probes the angle between the transition dipoles of the eigenstates; as we have seen (Fig. 4), this angle may be rather sensitive to structure.

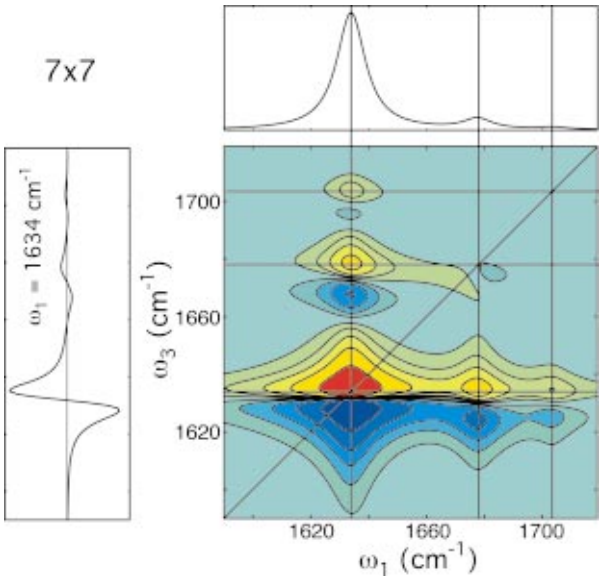

FIG. 7. (Color) Linear and 2DIR spectra as in Fig. 5 but for a 7×7 extended sheet with the slice taken along $\omega_1=1634\ \mathrm{cm}^{-1}$.

In addition to each of the positive diagonal and cross-peak features, the two-dimensional spectra in Figs. 5–7 indeed show the negative peaks shifted to lower frequency along the ω_3 axis, associated with the transitions from one-quantum states to two-quantum states (see Sec. III B). The shift results from the anharmonic nature of the oscillators. For the case of a single oscillator (not to be confused with the single unit cell), this shift would simply be given by A, i.e., 16 cm^{-1} for our parameter choice. For systems of N coupled oscillators, however, this shift will be reduced because the delocalized eigenstates have a small occupation probability, of the order of $1/N$, on each of the oscillators. As the anharmonic term in the Hamiltonian Eq. (1) basically adds the squares of the excitation probabilities on each of the oscillators, one expects the anharmonic shift to scale according to A/N (as long as this shift is larger than the homogeneous linewidth γ). The two-dimensional spectra in Figs. 5–7 indeed clearly show the decrease of the splitting between positive peaks and their associated negative peaks with increasing system size. We also see that the negative peaks form progressions of transitions along the ω_3 direction, tailing to lower energies. Within a perturbative treatment of the anharmonicity, the main induced-absorption peak results from a one-quantum excitation from the one-quantum excited state to create a two-quantum state that is the direct product of two one-quantum states. It should be kept in mind that the two-quantum states created in this manner are not proper eigenstates: their scattering on the anharmonic term in the Hamiltonian will mix the doubly excited state with other direct products of two one-quantum states, thus transferring induced absorption strength to them. This leads to a progression of induced-absorption peaks extending towards lower values of ω_3.

We next turn to a discussion of the effect of the periodic boundary conditions. To this end, we first consider Fig. 8, in which we give the linear spectra for a 3×1 hairpin and a 3×3 sheet, calculated with periodic boundary conditions (dashed lines) and open boundary conditions (solid lines). For the hairpin, the boundary conditions have very little effect, even for this very small system of only three unit cells (two strands of six oscillators). The spectrum is slightly shifted due to the edge effects of the open hairpin, but this shift is small compared to the imposed linewidth γ. Also, we do not see the $k=3$ satellite peaks arising on the main $a-$ and $a+$ peaks, because the dispersion constants $J_{\pm}^{a}$ (which set the scale for the energy differences between the main and satellite peaks) are small compared to γ. For a smaller choice

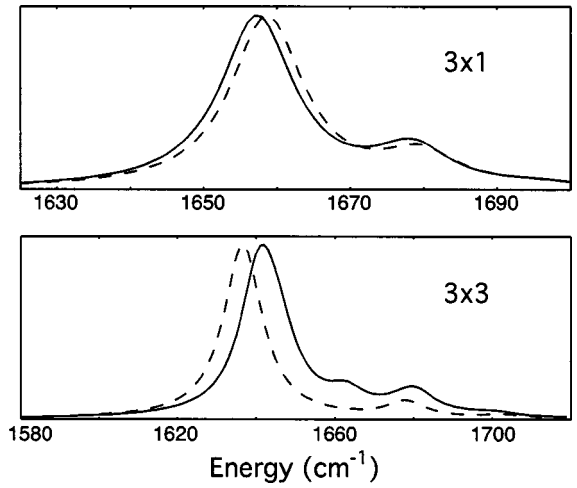

FIG. 8. Linear absorption spectra for a 3×1 hairpin (top) and a 3×3 extended sheet (bottom) calculated using periodic boundary conditions (dashed lines) and by brute-force diagonalization of the Hamiltonian for the finite system with open boundary conditions (solid lines).

of γ, the effects would look more dramatic, but this would not be typical for real proteins.

By contrast, for the 3×3 sheet (36 oscillators), the edge effects are much stronger. This result is a direct consequence of the stronger intercell interactions which exist in the extended sheet, leading to dispersion constants that are comparable to or larger than γ. As a result, we see appreciable differences in the positions of the two dominant peaks for periodic and open boundary conditions. Moreover, we see that open boundary conditions lead to an extra peak near 1663 cm^{-1}, which has an intensity similar to the $a+$-type peak. This peak should not be thought of as a simple satellite of one of the main peaks, because the intercell interactions in extended sheets are comparable to the splittings between the cell eigenstates $|a\pm\rangle$ and $|s\pm\rangle$. Hence all four types of cell states mix strongly, in particular in the center region of the spectrum. The transition dipole associated with the new peak makes a rather small angle (15°) with the strongest ($a-$ type) transition at 1641 cm^{-1}. The smallness of this angle results from the fact that the eigenstates acquire most of their oscillator strength from the $a-$ cell transitions. As the system size increases, the relative intensity of the extra peak decreases slightly, it shifts toward lower frequency and rotates to be nearly parallel to the large amplitude transition, yet the extra peak persists for large system sizes. The precise size where we can no longer identify the extra peak as a separate feature depends on the value of γ, but generally one can say that extended antiparallel β sheets have important finite-size effects that cannot be modeled using periodic boundary conditions.

To enhance the effect of the extra dipole-allowed transitions for open boundary conditions, we present in Fig. 9 the linear and two-dimensional spectra for the 3×3 sheet calculated using a smaller linewidth, $\gamma=2.5$ cm^{-1}, both for open boundary conditions and periodic ones. We can now even distinguish a fourth transition, as a blue shoulder of the main peak. The two-dimensional spectrum with open boundary conditions clearly shows cross peaks between the main transition at 1641 cm^{-1} and the two extra peaks. Of course, these cross peaks do not exist for periodic boundary conditions. Even if the linewidths were significantly larger, we could still identify these transitions in the two-dimensional spectrum. Again, we note that these finite-size effects for extended sheets, which are particularly visible in two-dimensional spectra, persist over a large range of sizes, up to systems of the order of 10×10 unit cells. At the present value of γ, we still find the extra peak for systems of 20×20 unit cells (1600 oscillators), even though the two major peaks corre-

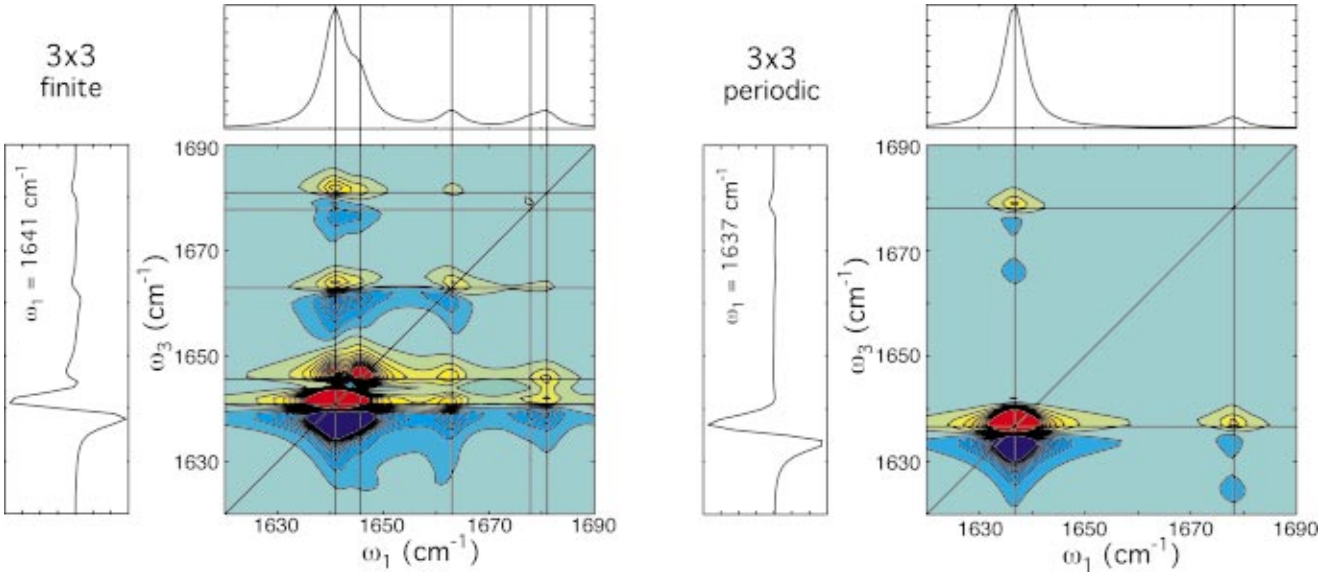

FIG. 9. (Color) Comparison of linear and 2DIR spectra calculated using open (left) and periodic (right) boundary conditions for a 3×3 extended sheet. For each set of spectra the linear spectrum is given across the top, the 2DIR contour plot is in the center, and a slice for a fixed value of ω_1, taken at the frequency corresponding to the strongest transition in the linear spectrum, is on the left. To enhance the effects of open boundary conditions, we have in this figure used a smaller Lorentzian linewidth parameter, $\gamma=2.5$ cm^{-1}, than the one used in Figs. 5–8.

spond almost exactly to those calculated using periodic boundary conditions.

To end this section we briefly mention some results for parallel β sheets, which, per unit cell, have two instead of four peptides, i.e., two amide I oscillators. Because the oscillators do not interact strongly, the splitting between the two cell eigenstates is small. One of the states carries most (98.6%) of the oscillator strength, so that the spectrum is dominated by one transition. Increasing the size of the system shifts the band, to higher frequency with increasing number of unit cells in the X direction and to lower frequency for extended sheets. As the linear spectra for parallel sheets involve only one transition, the two-dimensional spectra are rather trivial, dominated by one diagonal peak.

VI. CHOICE OF INTERACTION AND BROADENING MODELS

In our calculations, we have used the transition dipole coupling model to calculate the interactions between amide I oscillators in the sheet. This approach neglects the effects of orbital overlap and the breakdown of the point-dipole approximation for peptide units that are located close together. Because our methods for calculating spectra do not depend on the nature of the interactions, such effects are in principle easily included, but, to keep the model simple and the number of parameters small, we have used the simplest available model for the couplings. We are mostly interested in trends of the spectra as we change the size and structure of the sheets, and we believe that these trends are only weakly affected by the precise nature of the interactions. This belief is supported by our results for the one-quantum eigenstates, which as noted in section 4 are governed by the symmetry of the system.

It is difficult to accurately assess from first principles the factor C that scales the magnitude of the dipolar coupling Eq. (2). This factor is proportional to the squared magnitude of the transition dipole moment of the individual oscillators and inversely related to the dielectric constant of the medium. Although the magnitude of the transition dipole moment is known for isolated amides, the integration of the peptide unit into a regular secondary structure with significant hydrogen bonding may change this magnitude. Moreover, determining an effective dielectric constant for the local environment of protein and water is a very hard problem, which has no unique solution. These uncertainties complicate the choice of the parameter C. We use $C=580\ \mathrm{cm}^{-1}\ \text{Å}^3$, which is consistent with previously used values,[1,38] and results in a splitting between the peaks for the extended sheets that agrees with experiment.[2,4,32] We have checked that taking C a factor of 2 larger (smaller) does not change the trends observed in the calculated spectra, even though it does increase (decrease) the splittings between the various peaks.

More detailed studies of the couplings between amide I oscillators are an area of intense research at this time,[27–30,56,57] but presently there is little consensus on the best approach for treating the couplings in large complex protein or peptide systems. As noted in regards to the constant C, it is even difficult to establish a reliable set of parameters for the simplest approximation of point transition dipoles. Ultimately, the splittings between the eigenstates are determined by the largest interactions, which for β sheets occur between oscillators in different strands. Consequently, through-bond couplings, determined by the ϕ/ψ angles, affect only the very weak interactions within strands and are not very important for the wavefunctions and energies of the eigenstates. The fact that the strongest interactions occur between oscillators in different strands and separated by more than 3 Å suggests that the interactions are in the limit where transition dipole coupling works the best. In the absence of more detailed coupling models, we feel that the carefully parametrized transition dipole coupling model is acceptable because it gives coupling magnitudes consistent with the intuitive result that interstrand interactions are stronger than intra-strand interactions in antiparallel β sheets.

In our calculations, we have assumed a purely homogeneous broadening mechanism, governed by the linewidth γ. Within this model, the two-dimensional spectrum is rather simple and can essentially be predicted from the linear spectrum with some idea of the anharmonicity. This simple pattern is not present in experimentally measured two-dimensional spectra, because inhomogeneity (disorder in the fundamental oscillator frequencies and the interactions) broadens the transitions along the diagonal, and the positive and negative features of the diagonal peaks and the cross peaks interfere, leading to complex and unintuitive lineshapes. We note that for growing inhomogeneity, where the individual peaks in the linear spectrum run together, the cross peaks in the two-dimensional spectrum may still be more easily identified.

An important effect of inhomogeneity is that it breaks the translational symmetry of the system and tends to localize the eigenstates on a number of oscillators, N_{del} the delocalization length, smaller than N. The value for N_{del} depends on the ratio of the width of the inhomogeneous (energy and interaction) distribution to the one-quantum bandwidth, dictated by the dominant interactions. The exact dependence is a function of the interaction mechanism and the dimensionality, but the general trend is always that N_{del} decreases as the magnitude of the ratio increases.[55] As we have seen, for hairpins the bandwidths ($\sim 4J^a_{\pm}$) are small and in practice it is rather unlikely that the one-quantum eigenstates are delocalized over more than just a few peptide units. By contrast, for extended antiparallel sheets the bandwidths are appreciably larger and a stronger delocalization is to be expected, even in practice. It is of interest to note that, in principle, the splitting between the negative and associated positive contributions in the two-dimensional spectrum should scale like A/N_{del} (cf. Sec. V), which could offer a spectroscopic ruler for measuring N_{del}. For the delocalization length of excitons in molecular J aggregates, such a ruler is indeed provided by the pump-probe spectrum.[58] It will be of interest to investigate whether indeed a similar method can be applied for the more complicated case of anharmonic oscillators.

VII. MARKERS FOR STRUCTURE

The most important goal of this study is to identify characteristic spectral features that distinguish secondary struc-

tural elements of proteins. This goal motivated previous studies of linear infrared spectroscopy. Because the cross peaks in two-dimensional spectra more easily survive spectral congestion than features in the linear spectra, they provide new and significant structural markers. In addition, the cross peaks yield information concerning the coupling between vibrational states, i.e., about the spatial correlation of transitions. The fact that two-dimensional spectroscopy also probes the angle between the dipoles of transitions that contribute to cross peaks supplies further possibilities to distinguish structure. For β sheets one would like to distinguish parallel from antiparallel sheets and separate hairpins from extended sheets.

As mentioned briefly at the end of Sec. V, parallel β sheets have two oscillators per unit cell, resulting in two allowed transitions in the infrared spectrum. Because of the relatively weak interactions between the oscillators the two transitions are nearly degenerate, and one of the states has most of the intensity. Antiparallel sheets have four allowed transitions and two of them exhibit significant oscillator strength. The splitting between these two peaks varies from 20 to 40 cm^{-1} depending on the geometry of the sheet. The second peak distinguishes parallel from antiparallel sheets and has been identified before as a structural marker,[2,4,34,40,41] but it is sometimes difficult to clearly identify this peak due to spectral congestion.[38] As we argued, in two-dimensional spectra the cross peak between the two dominant transitions stands out clearly and thus serves as an indicator of antiparallel sheets, even if transitions from other secondary structures complicate the linear absorption spectrum. In addition, we have seen in Figs. 7 and 9 that cross peaks between the strongest transition near 1640 cm^{-1} and the high-frequency out-of-plane transition, near 1700 cm^{-1}, as well as transitions arising from the finite-size effects, are clearly visible in two-dimensional spectra for extended antiparallel β sheets. All these cross peaks are strong evidence of antiparallel β-sheet structure. Conversely, the absence of such peaks indicates that antiparallel sheet structure is not present, suggesting parallel sheets if there is other evidence of β-sheet structure.

We can also discern spectral differences between hairpins and extended sheets. The splitting between the two dominant transitions in the spectrum distinguishes these structures, because the main peak shifts to lower energy for extended sheets, approaching 1633 cm^{-1} for large sheets, and to higher energy for hairpin structures, approaching 1660 cm^{-1} for long hairpins. The cross peak position in ω_1 and ω_3 gives the positions of the constituent transitions. The angle between the transitions also distinguishes hairpins from sheets. The angle changes from 47° for hairpins to around 65° for extended sheets. The extra ''finite-size'' features that occur for extended antiparallel sheets are additional structural markers, as they do not exist for hairpins. These observations also explain why the empirical rules for the relationships between protein structure and spectroscopy fail for hairpins.[2,33] These rules were developed from measurements for many proteins, and proteins usually exhibit more extended sheet structures. The amide I spectra, however, are sensitive to the difference between hairpins and extended sheets.

It should be stressed that, due to the delocalized nature of the vibrational states, the infrared spectra do not reflect structural information with atomic resolution. Instead, amide I is a marker for protein secondary structure. In practice, disorder counteracts strong delocalization (see end of Sec. VI), and the spatial range that is probed varies. For hairpins, the states probably are rather localized in practice, making the spectra rather insensitive to their lengths. By contrast, for extended sheets the delocalization range N_{del} may be much larger and the spectra may reflect the size of the sheet. Numerical analysis of two-dimensional spectra including the effects of disorder will be needed to corroborate these statements.

VIII. CONCLUSIONS

We calculated the linear and two-dimensional amide I vibrational spectra for an idealized model of β sheets. The calculations reveal spectroscopic markers that separate parallel sheets from antiparallel sheets and distinguish hairpins $(N_x \times 1)$ from extended sheets $(N_x \times N_x)$. For hairpins, the results are almost insensitive to the choice of boundary conditions, while for extended sheets strong interactions between unit cells cause stronger finite-size effects. For extended sheets, extra peaks not present under periodic boundary conditions appear in the spectra with the, more appropriate, open boundary conditions, and the angle between the transition dipoles of the two dominant transitions is overestimated by using periodic boundary conditions. The two-dimensional infrared spectra show the expected features based on the linear spectra. There are positive cross peaks between each pair of one-quantum (linear) transitions, as well as more subtle negative features that arise from the effect of the anharmonicity on the two-quantum states. As suggested, the splitting between related positive and negative features in principle contains information on the delocalization of the vibrational states.

Our results for the infrared spectroscopy of β sheets agree with the empirical relationship between β-sheet secondary structure and amide I spectral features that have been used as structural markers in the past and also explain deviations from this relationship that have plagued the analysis of infrared spectra of β hairpins.[2,33] We have shown that interstrand interactions determine the splittings between the transitions of β-sheet spectra and not interactions between nearest neighbors along the strand as determined by the ϕ/ψ angles. We have also demonstrated that the symmetry of the unit cell dictates the intensity of the transitions and the angle between their dipoles.

ACKNOWLEDGMENTS

This work was supported by the National Science Foundation, the Petroleum Research Fund of the American Chemical Society, and the Packard Foundation. C.M.C. and A.T. acknowledge the support of the National Parkinson

Foundation. J.K. acknowledges hospitality and support from the Massachusetts Institute of Technology during the initial stage of this research.

[1] S. Krimm and J. Bandekar, Adv. Protein Chem. **38**, 181 (1986).
[2] M. Jackson and H. H. Mantsch, Crit. Rev. Biochem. Mol. Biol. **30**, 95 (1995).
[3] T. F. Kumosinski and J. J. Unruh, Talanta **43**, 199 (1996).
[4] W. K. Surewicz, H. H. Mantsch, and D. Chapman, Biochemistry **32**, 389 (1993).
[5] M. Khalil, N. Demirdöven, and A. Tokmakoff, J. Phys. Chem. B. **107**, 5258 (2003).
[6] S. Mukamel, Annu. Rev. Phys. Chem. **51**, 691 (2000).
[7] M. T. Zanni, S. Gnanakaran, J. Stenger, and R. M. Hochstrasser, J. Phys. Chem. B **105**, 6520 (2001).
[8] M. Khalil and A. Tokmakoff, Chem. Phys. **266**, 213 (2001).
[9] O. Golonzka, M. Khalil, N. Demirdöven, and A. Tokmakoff, Phys. Rev. Lett. **86**, 2154 (2001).
[10] O. Golonzka, M. Khalil, N. Demirdöven, and A. Tokmakoff, J. Chem. Phys. **115**, 10814 (2001).
[11] R. M. Hochstrasser, M. C. Asplund, P. Hamm, and N. H. Ge, J. Chin. Chem. Soc. (Taipei) **47**, 843 (2000).
[12] M. T. Zanni, N. H. Ge, Y. S. Kim, and R. M. Hochstrasser, Proc. Natl. Acad. Sci. U.S.A. **98**, 11265 (2001).
[13] O. Golonzka and A. Tokmakoff, J. Chem. Phys. **115**, 297 (2001).
[14] S. Woutersen, R. Pfister, P. Hamm, Y. G. Mu, D. S. Kosov, and G. Stock, J. Chem. Phys. **117**, 6833 (2002).
[15] R. M. Hochstrasser, N. H. Ge, S. Gnanakaran, and M. T. Zanni, Bull. Chem. Soc. Jpn. **75**, 1103 (2002).
[16] N. H. Ge and R. M. Hochstrasser, PhysChemComm **5**, 17 (2002).
[17] N. Demirdöven, M. Khalil, and A. Tokmakoff, Phys. Rev. Lett. **89**, 237401 (2002).
[18] S. Woutersen, Y. G. Mu, G. Stock, and P. Hamm, Proc. Natl. Acad. Sci. U.S.A. **98**, 11 254 (2001).
[19] N. Demirdöven, M. Khalil, O. Golonzka, and A. Tokmakoff, J. Phys. Chem. A **105**, 8025 (2001).
[20] S. Woutersen and P. Hamm, J. Phys.: Condens. Matter **14**, R1035 (2002).
[21] M. T. Zanni and R. M. Hochstrasser, Curr. Opin. Struct. Biol. **11**, 516 (2001).
[22] S. Woutersen and P. Hamm, J. Chem. Phys. **114**, 2727 (2001).
[23] S. Woutersen and P. Hamm, J. Chem. Phys. **115**, 7737 (2001).
[24] S. Woutersen and P. Hamm, J. Phys. Chem. B **104**, 11316 (2000).
[25] P. Hamm, M. Lim, W. F. DeGrado, and R. M. Hochstrasser, J. Chem. Phys. **112**, 1907 (2000).
[26] P. Hamm, M. H. Lim, and R. M. Hochstrasser, J. Phys. Chem. B **102**, 6123 (1998).
[27] P. Hamm and S. Wouterson, Bull. Chem. Soc. Jpn. **75**, 985 (2002).
[28] S. Ham and M. Cho, J. Chem. Phys. **118**, 6915 (2003).
[29] S. Y. Cha, S. H. Ham, and M. H. Cho, J. Chem. Phys. **117**, 740 (2002).
[30] H. Torii and M. Tasumi, J. Raman Spectrosc. **29**, 81 (1998).
[31] R. Silva, S. C. Yasui, J. Kubelka, F. Formaggio, M. Crisma, C. Toniolo, and T. A. Keiderling, Biopolymers **65**, 229 (2002).
[32] J. Hilario, J. Kubelka, F. A. Syud, S. H. Gellman, and T. A. Keiderling, Biopolymers **67**, 233 (2002).
[33] J. Kubelka and T. A. Keiderling, J. Am. Chem. Soc. **123**, 12048 (2001).
[34] T. Miyazawa, J. Chem. Phys. **32**, 1647 (1960).
[35] T. Miyazawa and E. R. Blout, J. Am. Chem. Soc. **83**, 712 (1961).
[36] J. Bandekar and S. Krimm, Biopolymers **27**, 885 (1988).
[37] J. Bandekar and S. Krimm, Biopolymers **27**, 909 (1988).
[38] H. Torii and M. Tasumi, J. Chem. Phys. **96**, 3379 (1992).
[39] N. A. Nevskaya and Y. N. Chirgadze, Biopolymers **15**, 637 (1976).
[40] Y. N. Chirgadze and N. A. Nevskaya, Biopolymers **15**, 607 (1976).
[41] Y. N. Chirgadze and N. A. Nevskaya, Biopolymers **15**, 627 (1976).
[42] J. A. Leegwater and S. Mukamel, Phys. Rev. A **46**, 452 (1992).
[43] V. Chernyak, N. J. Wang, and S. Mukamel, Phys. Rep. **263**, 213 (1995).
[44] W. M. Zhang, V. Chernyak, and S. Mukamel, J. Chem. Phys. **110**, 5011 (1999).
[45] G. Juzeliunas and J. Knoester, J. Chem. Phys. **112**, 2325 (2000).
[46] M. Bednarz and J. Knoester, J. Phys. Chem. B **105**, 12913 (2001).
[47] C. Didraga, J. A. Klugkist, and J. Knoester, J. Phys. Chem. B **106**, 11474 (2002).
[48] C. L. Nesloney and J. W. Kelly, Bioorgan. Med. Chem. **4**, 739 (1996).
[49] M. T. Zanni, M. C. Asplund, and R. M. Hochstrasser, J. Chem. Phys. **114**, 4579 (2001).
[50] A. S. Davydov, *Theory of Molecular Excitons* (Plenum, New York, 1971).
[51] S. Mukamel, *Principles of Nonlinear Optical Spectroscopy* (Oxford University Press, New York, 1995).
[52] M. Khalil, N. Demirdöven, and A. Tokmakoff, Phys. Rev. Lett. **90**, 047401 (2003).
[53] C. Scheurer and S. Mukamel, J. Chem. Phys. **115**, 4989 (2001).
[54] J. Y. Sung and R. J. Silbey, J. Chem. Phys. **115**, 9266 (2001).
[55] H. Fidder, J. Knoester, and D. A. Wiersma, J. Chem. Phys. **95**, 7880 (1991).
[56] J. H. Choi, S. Ham, and M. Cho, J. Chem. Phys. **117**, 6821 (2002).
[57] H. Sihyun, C. Sangyob, J. H. Choi, and M. Cho, J. Chem. Phys. **119**, 1451 (2003).
[58] L. D. Bakalis and J. Knoester, J. Phys. Chem. B **103**, 6620 (1999).